



Sea urchin-like NiCoO₂@C nanocomposites for Li-ion batteries and supercapacitors

Jin Liang^{a,1}, Kai Xi^{b,1}, Guoqiang Tan^{c,1}, Sheng Chen^a, Teng Zhao^b, Paul R. Coxon^b, Hyun-Kyung Kim^b, Shujiang Ding^{a,*}, Yuan Yang^d, R. Vasant Kumar^b, Jun Lu^{c,*}

^a Department of Applied Chemistry, School of Science, State Key Laboratory for Mechanical Behavior of Materials, Xi'an Jiaotong University, Xi'an 710049, China

^b Department of Materials Science and Metallurgy, University of Cambridge, Cambridge CB3 0FS, UK

^c Chemical Sciences and Engineering Division, Argonne National Laboratory, Argonne, IL 60439, USA

^d Materials Science and Engineering, Department of Applied Physics and Applied Mathematics, Columbia University, NY 10027, USA

ARTICLE INFO

Article history:

Received 22 February 2016

Received in revised form

13 June 2016

Accepted 18 June 2016

Available online 13 July 2016

Keywords:

NiCoO₂

Hollow concave carbon

Electrochemistry

Lithium ion battery

Supercapacitor

ABSTRACT

The rational construction of battery electrode architecture that offers both high energy and power densities on a gravimetric and volumetric basis is a critical concern but achieving this aim is beset by many fundamental and practical challenges. Here we report a new sea urchin-like NiCoO₂@C composite electrode architecture composed of NiCoO₂ nanosheets grown on hollow concave carbon disks. Such a unique structural design not only preserves all the advantages of hollow structures but also increases the packing density of the active materials. NiCoO₂ nanosheets grown on carbon disks promote a high utilization of active materials in redox reactions by reducing the path length for Li⁺ ions and for electron transfer. Meanwhile, the hollow concave carbon not only reduces the volume change, but also improves the volumetric energy density of the entire composite electrode. As a result, the nanocomposites exhibit superior electrochemical performance measured in terms of high capacity/capacitance, stable cycling performance and good rate capability in both Li-ion battery and supercapacitor applications. Such nanostructured composite electrode may also have great potential for application in other electrochemical devices.

© 2016 Published by Elsevier Ltd.

1. Introduction

Various electrochemical energy storage and conversion systems are becoming more appealing than ever due to the imminent shortage of fossil fuels and the rapid exhaustion of non-renewable resources [1–3]. As significant electric energy storage devices, Li-ion batteries (LIBs) and supercapacitors (SCs) are attracting worldwide interest spurred on by the demands of lightweight and reliable power sources for portable electronics, stationary energy storage and hybrid electric vehicles (HEVs) [4–7]. Nonetheless, these devices need a considerable improvement for meeting the requirements of electrical vehicle applications and also for high energy storage and portable electronics. Transition metal oxides (TMOs) have been extensively used as functional materials in such diverse fields as fuel cells, LIBs and ECs [6,8,9]. TMOs with two different metal cations display higher electrochemical activities

and higher electrical conductivities than simple TMOs [10,11]. For example, binary NiCoO_x have attracted much attention as electrode materials in both LIBs and ECs due to their inherent electrochemical advantages, low cost, abundant availability, and environmental benignity [6,12–14]. Moreover, NiCoO_x exhibit higher specific capacity/capacitance than that of corresponding monometal oxides by generating two active metallic components accompanied by the relatively low activation energy for electron transfer between the two cations and the resulting metals [10,15]. However, the development of binary oxide electrodes with good cycling performance has been beset by problems arising from the poor electron/ion conduction TMOs and pulverization during charging-discharging [16].

To address these issues, various NiCoO_x nanostructures have been investigated, including nanoparticles [17], nanosheets [18], nanoplatelets [19], nanowires [20], nanotubes [6] and nanoflakes [21], resulting in generally improved electrochemical performances, which are attributed to the unique electrode properties manifest at the nanoscale, including enhanced active surface area, short ion diffusion pathways and better accommodation of the

* Corresponding authors.

E-mail addresses: dingsj@mail.xjtu.edu.cn (S. Ding), junlu@anl.gov (J. Lu).

¹ These authors contributed equally to this work.

strains from volume changes. Recently, the formation of nanocomposites with nanostructured carbonaceous allotropes, such as amorphous carbon [22,23], ordered microporous carbon [24], graphene [25] and carbon nanotubes [26], have been widely explored. High electrical conductivity, flexibility, and chemical stability of carbonaceous materials are found to serve as cushions to alleviate cyclic stress as well as to act as scaffolds for active nanoparticles to help shorten the ionic diffusion path [27]. It is noted that nanosheet composites with hollow structured carbon, such as nanospheres, nanotubes and nanocubes, demonstrated improved energy storage performance, especially improved cycling stability from their ability to better sustain the volume variations during cycling [28,29].

A typical drawback of electrodes fabricated with such hollow spheres is that they normally suffer from comparatively low volumetric energy and power densities. These are caused by the large empty spaces between and inside the hollow spheres arising from poor packing of the particles and thus the increase the demand for larger amount of electrolyte to infiltrate the space [7,27]. Here, we report on the design of an advanced electrode architecture consisting of ultrathin NiCoO₂ nanosheets (NSs) grown on a hollow single concave carbon disk with these arranged topographically in space to decrease the excessive hollow interior space while maintaining the general merits of hollow structures.

As displayed in Fig. 1, there are three aspects that we could not ignore for energy storage devices requiring to provide both high specific gravimetric and volumetric energy densities. The morphology presented here can be described as follows. Imagine a deflated porous spherical ball which is then pressed in from one end to form a hollow single concave structure. This modification will allow the particles to closely pack, when compared with the original sphere thus giving rise to increased packing density [30,31] and enhancing volumetric energy density for the same surface area [7,32]. Additionally, the compact arrangement of the concave architecture results in a better balanced electrolyte

distribution at decreased amounts in direct comparison with the use of the simple spherical material shape. The carbon itself retains its porosity both within the concave structure and at the outer surface for directly participating in intercalation of Li. Also, the ultrathin nanosheet and surface porosity can better accommodate the strain from volume changes on lithiation of the oxide and the ensuing metal particle sheets. The distances required for transfer of ions and electrons are greatly reduced which can further enhance the supply of electroactive sites [33–35]. In summary, the sea urchin-like NiCoO₂ NSs@C nanocomposite can provide shorter path lengths for electronic transport and more diffusion paths for ionic transport in the electrolyte in comparison with carbon hollow spheres [36]. As anticipated, in view of the above-mentioned superior properties, the sea urchin-like NiCoO₂ NSs@C composites displayed high specific capacity and capacitance, enhanced rate capability, and good cycling stability in both the lithium ion cell and the supercapacitor applications when compared with electrodes based upon spherical NiCoO₂ NSs@C composites. The improved electrochemical performance is based on packing of more active materials per unit volume, which can enable potential applications in energy storage devices demanding both high energy and high power.

2. Results and discussion

The synthesis process and the resulting electrode structure are schematically illustrated in Fig. S1 (Supporting information). A hollow polystyrene (PS) disk with a single concavity was sulfonated with concentrated sulfuric acid, to produce sulfonated polystyrene (SPS) particles. The SPS particles act as a supporting backbone to control the growth of ultrathin NiCoO₂ NSs for providing oxide precursor in the electrode. Sodium citrate was introduced to control the pH level in the solution, a defined Ni–Co precursor NSs could be easily loaded on the uniformly assembled

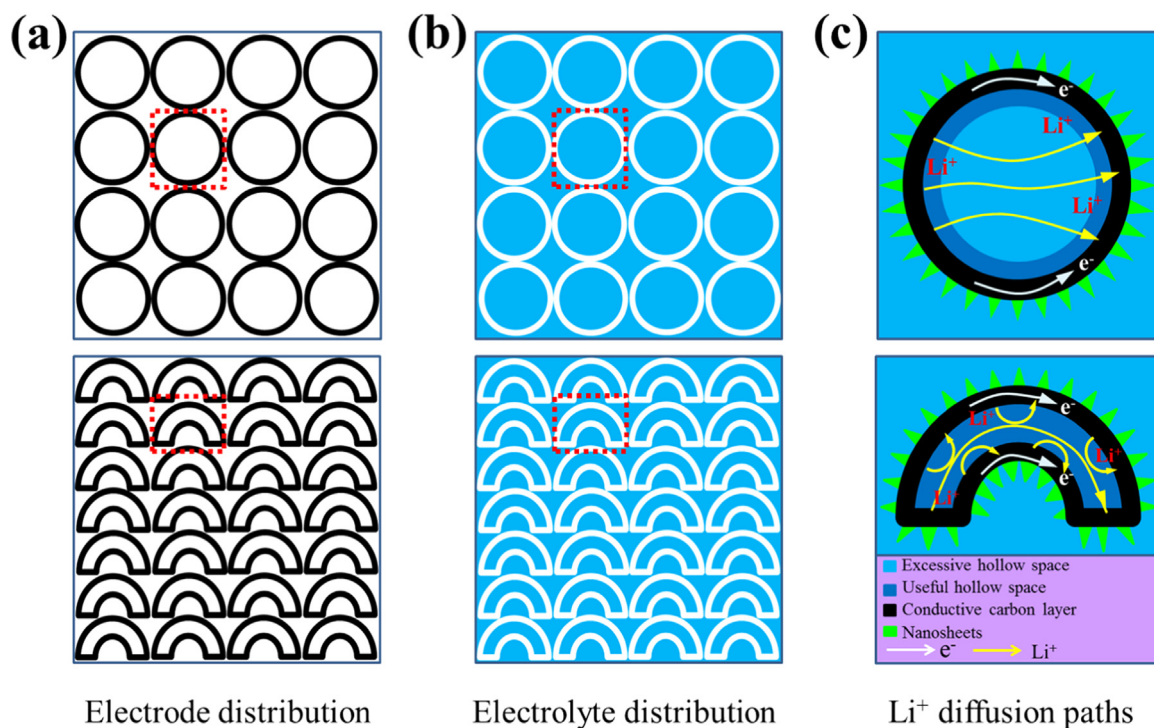
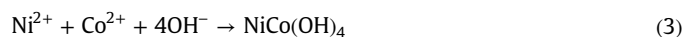
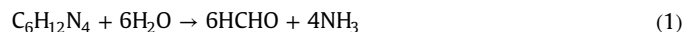


Fig. 1. Schematic illustration emphasizing the difference between the spherical and sea urchin-like particles in electrolyte distribution and conducting paths. (a) The black section is porous carbon segment; (b) The blue section is electrolyte both outside and inside the hollow carbon; (c) Li⁺ conducting paths are decreased, while electron connectivity is improved both accompanied in a better packed structure.

hollow concave SPS at temperatures $< 90\text{ }^{\circ}\text{C}$, as described by the following three chemical reactions:



In the above reaction sequence, amine was used as a source of ammonia in order to provide the hydroxyl ions to precipitate the binary metal hydroxide precursor. An heat treatment at $450\text{ }^{\circ}\text{C}$ in nitrogen is used to convert the Ni–Co precursor into NiCoO_2 as described by the simple calcination in reaction (4). In this procedure, the binary metal oxide is advantageously formed into nanosheets (NSs) supported on the outer surfaces of the carbon:



The morphology of the as-prepared samples was examined by field-emission scanning electron microscopy (FESEM) and transmission electron microscopy (TEM). In Fig. 2a and b, the hollow PSs have well-defined structures with diameters around $1\text{ }\mu\text{m}$. Fig. 2c and d show the uniform NiCoO_2 NSs@C spheres that all PSs are virtually covered by NiCoO_2 nanosheets. As a result of applying

a drying procedure to an emulsion of the hollow PS spheres, these are transformed by capillary forces into hollow concave PSs. It is clearly demonstrated that the hollow single concave disk-like particles are also highly uniform in diameter (identical to the diameter of the PSs) and with relatively smooth surfaces (Figs. 2e and S2a). After being treated with concentrated sulfuric acid, the concave shapes are sulfonated. Fig. 2f has testified that the sulfonated particles mostly preserved the hollow concave structure with a smooth surface. Fig. S2b provides evidence for the presence of a unique double layer in the hollow construction with defined cavity in the center of the disk. In the next step, the Ni–Co binary oxide precursor is then grown on the surface of the SPSs via a facile co-precipitation method (Fig. 2g and h), which is then annealed at $450\text{ }^{\circ}\text{C}$ for 3 h in nitrogen in order to form the NiCoO_2 which forms a coating as a nanosheet on each of the sulfonated polystyrene surface with the thickness of the NiCoO_2 nanosheets being around 3–6 nm (Fig. S3). The final morphology that was obtained can be best described as sea urchin-like NiCoO_2 NSs@C composites. The sea urchin-like NiCoO_2 NSs@C composites preserve the concave shape of the template (Fig. 2i), thus proving the excellent structural stability during chemical precipitation and annealing treatments. A key feature that stands out as depicted in Fig. 2j is that the constructed shape is hollow with shorter electrolyte paths, thus offering faster ionic diffusion and increased rate

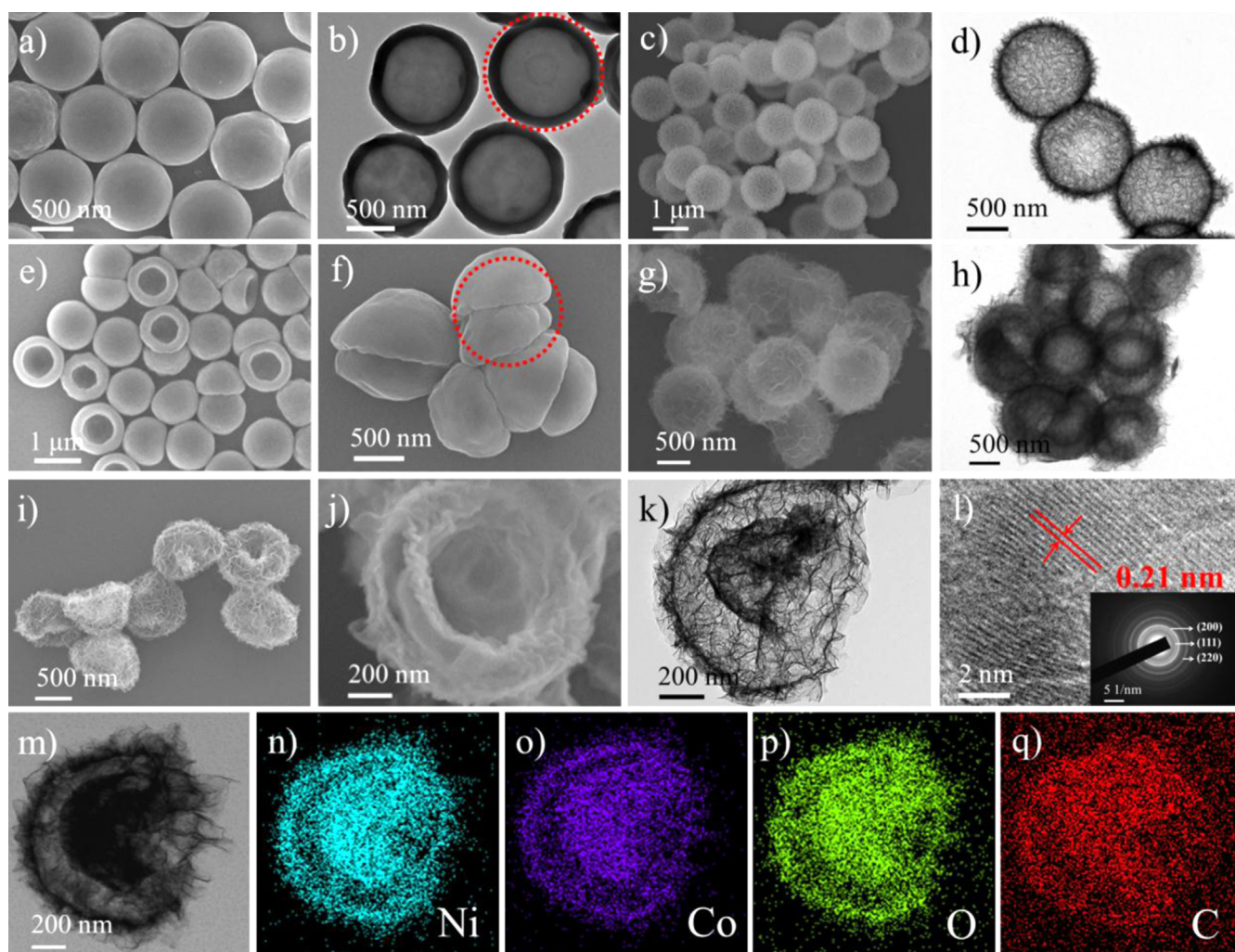


Fig. 2. SEM (a) and TEM (b) images of polystyrene microspheres; SEM (c) and TEM (d) images of spherical NiCoO_2 @C composites; SEM images of hollow concave polystyrene particles (e) and sulfonated polystyrene particles (f); SEM (g) and TEM (h) images of Ni–Co precursor@SPS composites; SEM (i and j), TEM (k), HRTEM (l) and SEAD (inserted l) images of representative sea urchin-like NiCoO_2 NSs@C hybrid materials; Elemental mapping images (n–q) of an individual sea urchin-like NiCoO_2 NSs@C particle shown in (m).

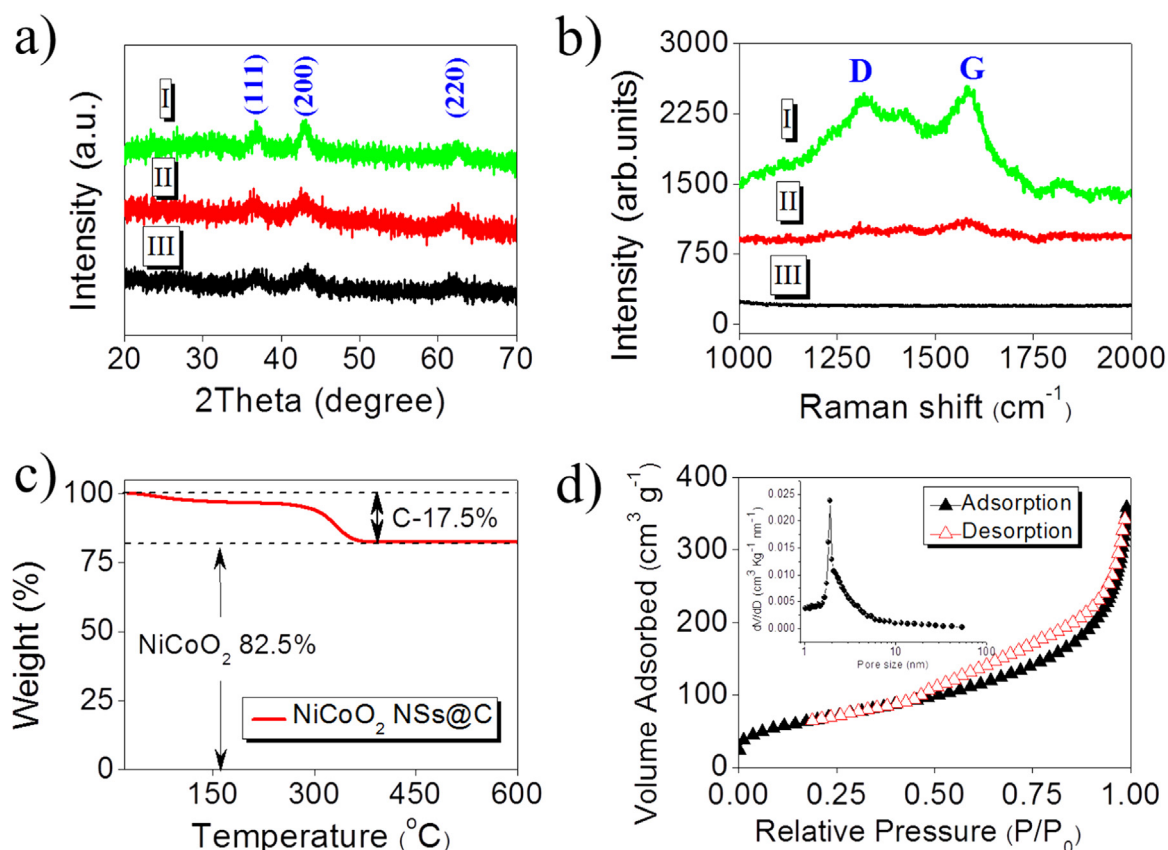


Fig. 3. (a) XRD patterns of block NiCoO₂ (I), sea urchin-like NiCoO₂ NSs@C (II) and NiCoO₂ NSs@C spheres (III); (b) Raman spectra of sea urchin-like NiCoO₂ NSs@C (I), NiCoO₂ NSs@C spheres (II) and block NiCoO₂ (III); (c) TGA analysis of sea urchin-like NiCoO₂ NSs@C; (d) N₂ adsorption-desorption isotherms of sea urchin-like NiCoO₂ NSs@C composites (the inset shows the pore-size distribution calculated from the adsorption branch).

of electrode reactions. Fig. 2k provides the proof that the composite has a porous morphology. As given in a representative high resolution TEM image (Fig. 2l), the measured interplanar distance (0.21 nm) corresponds to the (200) facet of NiCoO₂ [37]. The selected area electron diffraction (SAED) pattern (inserted in Fig. 2l) has confirmed the polycrystalline nature of the NiCoO₂ nanosheets. In addition, the diffraction rings are readily assigned to the NiCoO₂ phase [37]. The sea urchin-like NiCoO₂ NSs@C composites are further analysed by energy-dispersive X-ray spectroscopy (EDX) elemental mapping. As shown in Fig. 2m–q, the carbon is in the core of the material, while the shell consists of Co and Ni, which gives further evidence for the uniform growth of NiCoO₂ nanosheets on hollow concave carbon disks.

The obtained materials are characterized by X-ray diffraction (XRD) to identify the crystallographic structure. Fig. 3a shows the XRD patterns of block NiCoO₂ (I), sea urchin-like NiCoO₂ NSs@C (II) and NiCoO₂ NSs@C spheres (III). All of the diffraction peaks could be indexed to the cubic NiCoO₂ phase (JCPDS card no. 10-0188) with no other peaks being detected, indicating good phase purity of the binary oxides and the presence of amorphous carbon in both II and III samples [38]. Raman spectroscopy is used to characterize the carbon in the samples. In Fig. 3b, the two peaks (at ~1325 and 1587 cm⁻¹) corresponding to a high D/G ratio of sample I (sea urchin-like NiCoO₂ NSs@C) and sample II (NiCoO₂ NSs@C spheres) confirm that carbon in these materials is disordered such that XRD intensity is not visible [39]. However, the G peaks confirm that the presence of graphitic layers within the disordered carbon can help to reversibly intercalate Li⁺ in the electrode during charging. Thermogravimetric analysis (TGA) is applied to optimize the calcination temperature and to estimate the carbon content in the composite. Fig. 3c shows the thermal

decomposition process of sea urchin-like NiCoO₂ NSs@C composite. After reaching 600 °C at which carbon is expected to be oxidized away, the total weight of the remaining material is 82.5%, thus the weight fraction of carbon in the composite is calculated as 17.5%. The nitrogen adsorption/desorption isotherm of sea urchin-like NiCoO₂ NSs@C composites indicates a typical type III curve with a type H3 hysteresis loop [39], as displayed in Fig. 3d. A Brunauer–Emmett–Teller (BET) specific surface area of 244 m² g⁻¹ is obtained arising from the rather high proportion of mesopores (~4.6 nm, inset of Fig. 3d) present in the NiCoO₂ nanosheets and the close packing of the concave structure. Thus while the total surface area is unchanged, the addition of mesopore related surface area – which is electrochemically very useful – has shown a great increase. The detailed elemental composition and the oxidation state of the sea urchin-like NiCoO₂ NSs@C samples are further characterized by XPS measurements in Fig. S4. Fig. S4a gives the survey XPS spectrum of the sea urchin-like NiCoO₂ NSs@C, which shows it to mainly comprise carbon (C 1s), oxygen (O 1s), nickel and cobalt, and the absence of other impurities. Fig. S4b is the Ni 2p XPS spectrum which displays two major peaks with binding energy at 855.4 and 873.8 eV, corresponding to Ni 2p 3/2 and Ni 2p 1/2, respectively. The two satellite peaks at 861.8 and 880.2 eV are due to Ni shakeup at the high binding energy side of the Ni 2p 3/2 and Ni 2p 1/2. The high-resolution scan of Co 2p of the sample (Fig. S4c) exhibits two peaks at 781.1 and 796.9 eV, which can be assigned to the electronic state of Co 2p 3/2 and Co 2p 1/2, respectively, and the two couple of shakeup satellites. Therefore, we can state with high confidence the chemical composition of NiCoO₂ mesoporous nanosheets contains Ni²⁺, Ni³⁺, Co²⁺ and Co³⁺ ions which is in good agreement with previous results [40,41].

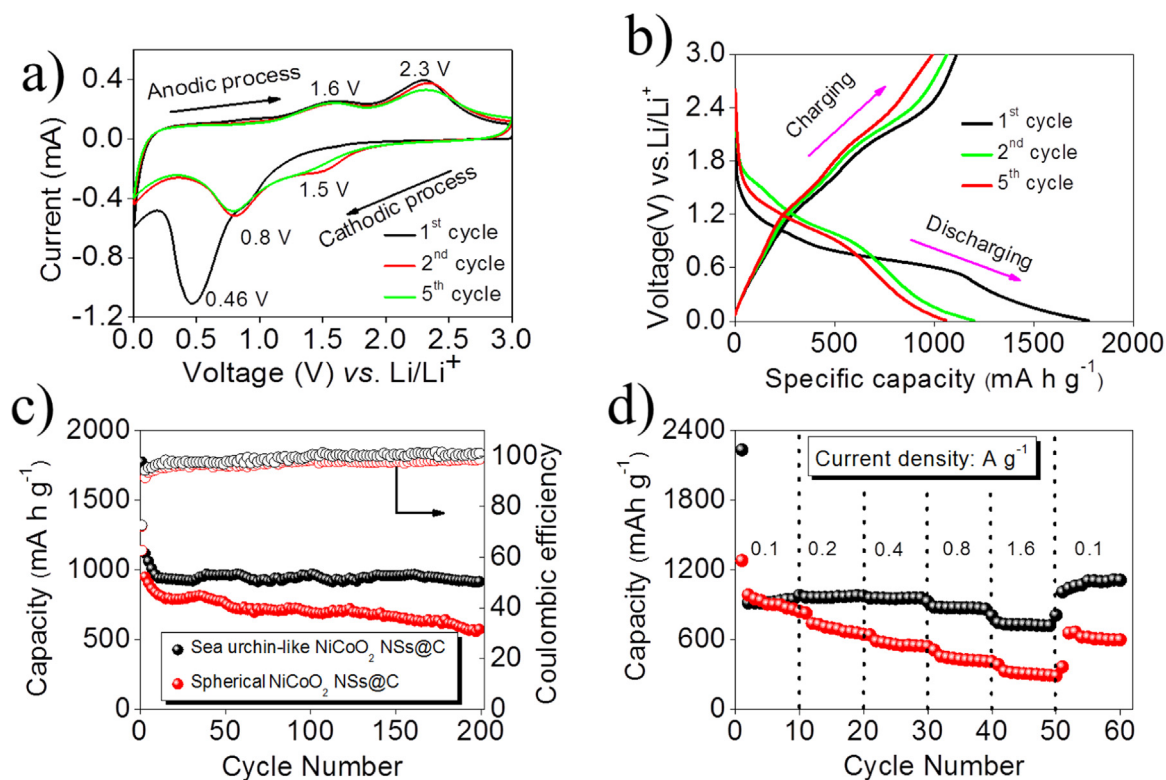


Fig. 4. (a) Cyclic voltammograms of sea urchin-like NiCo₂O₂ NSs@C composites at a scan rate of 0.5 mV s⁻¹; (b) Charge-discharge voltage profiles of sea urchin-like NiCo₂O₂ NSs@C composites at a current density of 0.4 A g⁻¹; (c) Cycling performances of sea urchin-like and spherical NiCo₂O₂ NSs@C composites; (d) Rate performance of sea urchin-like and spherical NiCo₂O₂ NSs@C composites at different current densities between 0.01 and 3.0 V.

To ascertain the benefits of using sea urchin-like NiCo₂O₂ NSs@C composites, we have investigated their electrochemical properties as an electrode material for LIBs. Fig. 4a shows the cyclic voltammograms (CVs) of the hybrid material for the 1st, 2nd, and 5th cycles in the potential range of 0.01–3.0 V at a scanning rate of 0.5 mV s⁻¹. The peak in the first cathodic scan at 0.7–0.8 V can be assigned to the decomposition of NiCo₂O₂ into Ni and Co ions [42]. The peaks at around 0.46 V and 0.02 V are attributed to the reduction of Ni/Co ions and carbon to Ni⁰/Co⁰ (Eq. (5)) [43] and Li_xC [44] as well as simultaneously the irreversible decomposition of the electrolyte as a solid electrolyte interface (SEI) layer. During the following anodic sweep, the two peaks at around 1.6 V and 2.3 V are attributed to the oxidation of Ni⁰ to Ni²⁺ and Co⁰ to Co²⁺. In the subsequent cycles, the main reduction peaks are shifted to higher potentials at 1.5 V and 0.8 V, which might be originate from the pulverization of the NiCo₂O₂ [45]. There is no significant change in the potentials of the oxidation peaks at ca. 1.6 V and 2.3 V (Eqs. (7) and (8)), respectively [46].

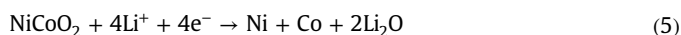


Fig. 4b gives the charge-discharge voltage curves cycled at a current density of 0.4 A g⁻¹ in a voltage range of 0.01–3.0 V vs. Li/Li⁺. In the charge-discharge profiles, poorly defined plateau regions can be observed which are consistent with the CV results above. The initial discharge and charge specific capacities are 1776 and 1114 mA h g⁻¹, respectively, based on the whole weight of the resulting hybrid material. It should be noted that the reversibility

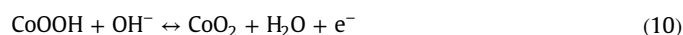
is significantly enhanced with an average Coulombic efficiency of 62.7%, 88.6% and 93.5% from the first, second and fiftieth cycles, demonstrating that the formed SEI during the subsequent cycles is stable and electrochemically favorable. The low initial Coulombic efficiency (CE) can be improved by surface coating or modification [47,48] and is left for future work. Impressively, the discharge capacity after 200 full charge/discharge cycles (Fig. 4c) is still as high as 913 mA h g⁻¹ at a current density of 0.4 A g⁻¹, which is 76% of that of the second cycle (1201 mA h g⁻¹). For comparison, the hollow NiCo₂O₂ NSs@C spheres and block NiCo₂O₂ materials have been tested under identical conditions. After 200 cycles, the remaining capacity of NiCo₂O₂ NSs@C spheres is 574 mA h g⁻¹ (Fig. 4c) and for the block material is only 184 mA h g⁻¹ (Fig. S5), both exhibiting relatively fast capacity fading. Similarly, the Coulombic efficiency and the volumetric specific capacity (Table S1) of sea urchin-like composites are superior to the hollow spherical material. After 200 cycles, a reversible volumetric specific capacity of the urchin-like NiCo₂O₂ NSs@C remained high at 885 mA h cm⁻³ while a capacity of spherical NiCo₂O₂ NSs@C was only 476 mA h cm⁻³.

The sea urchin-like NiCo₂O₂ NSs@C composites also showed better rate performance. Fig. 4d demonstrates the rate capacity of the samples at room temperature with increasing charge/discharge current densities successively. With increasing current densities from 0.1 to 1.6 A g⁻¹, the sea urchin-like NiCo₂O₂ NSs@C composites demonstrate a higher capacity than that of the hollow NiCo₂O₂ NSs@C spheres. When the current density is returned to 0.1 A g⁻¹, the sea-urchin like hybrid still exhibited a discharge capacity of 1111 mA h g⁻¹ after 60 cycles. Cycling at the same current density, the hollow NiCo₂O₂ NSs@C spheres based electrode fades to 599 mA h g⁻¹ as the current density drops back to 0.1 A g⁻¹. Clearly, the unique structure of sea urchin-like NiCo₂O₂ complex structures is beneficial for enhanced lithium storage properties. In particular, the existence of ultrathin nanosheets and

pores is especially beneficial for Li^+ diffusion within the electrolyte by shorter paths, resulting in better capacity and rate capability. Additionally, the special sea urchin-like and hollow concave conductive interior structure has the greater ability to buffer the large volume variation associated with the Li^+ insertion/extraction processes, thus relieving the pulverization issue associated with the phase changes of metal to oxides and vice versa and improving the cycling stability. To further investigate charge transfer and Li^+ diffusion kinetics in the samples, the electrochemical impedance spectroscopy (EIS) was used for the three samples. The results after the first cycle are shown in Fig. S6 [49]. The plots consist of a semicircle in the high-frequency region and a sloped straight line in the low frequency region. The semicircle is assigned to the charge-transfer resistance of the electrode/electrolyte interface while the inclined line corresponds to solid state diffusion of Li^+ into the bulk of the electrode material. The simulated electrochemical parameters are given in Table S2 by using the equivalent circuit in Fig. S6, in which R_s is solution resistance, R_{ct} is charge-transfer resistance, W_o is assigned to the semi-infinite Warburg diffusion impedance in the bulk. The diameter of the semicircle in the high-frequency of the sea urchin-like NiCoO_2 NSs@C electrode is smaller than that of the spherical NiCoO_2 NSs@C and aggregated NiCoO_2 NSs samples, indicating a lower charge-transfer resistance (32.9Ω) value for the structure proposed in this paper. The sea urchin-like NiCoO_2 NSs@C electrode can also offer a lower Warburg diffusion impedance (14.5Ω) than

that of spherical NiCoO_2 NSs@C at 35.5Ω . Therefore, the results from EIS show that the proposed sea urchin-like electrode offers rapid electron/ion transport during the electrochemical Li insertion/extraction reaction, leading to excellent electrochemical performances.

The sea urchin-like NiCoO_2 NSs@C composites are also suitable for use as an electrode material in a supercapacitor. The pseudocapacitive properties of sea urchin-like NiCoO_2 NSs@C composites are demonstrated by CV and galvanostatic charge-discharge measurements in three electrode configurations. In Fig. 5a, the typical CV curves of the hybrid electrode at different scan rates ranged from 8 to 50 mV s^{-1} . Particularly, a pair of redox peaks which have survived within 0–0.45 V (vs SCE) are displayed in all the curves, which can be referred to the Faradaic redox reactions related to M-O/M-O-OH (M refers to Ni or Co) [42]. The possible redox reactions in the alkaline electrolyte are based on the equation below [50,51].



The curve shapes show negligible changes as the scan rate is increased from 8 to 50 mV s^{-1} , demonstrating this material allows for fast redox reactions [6]. Galvanostatic charge-discharge measurement was used to further evaluate the pseudocapacitive

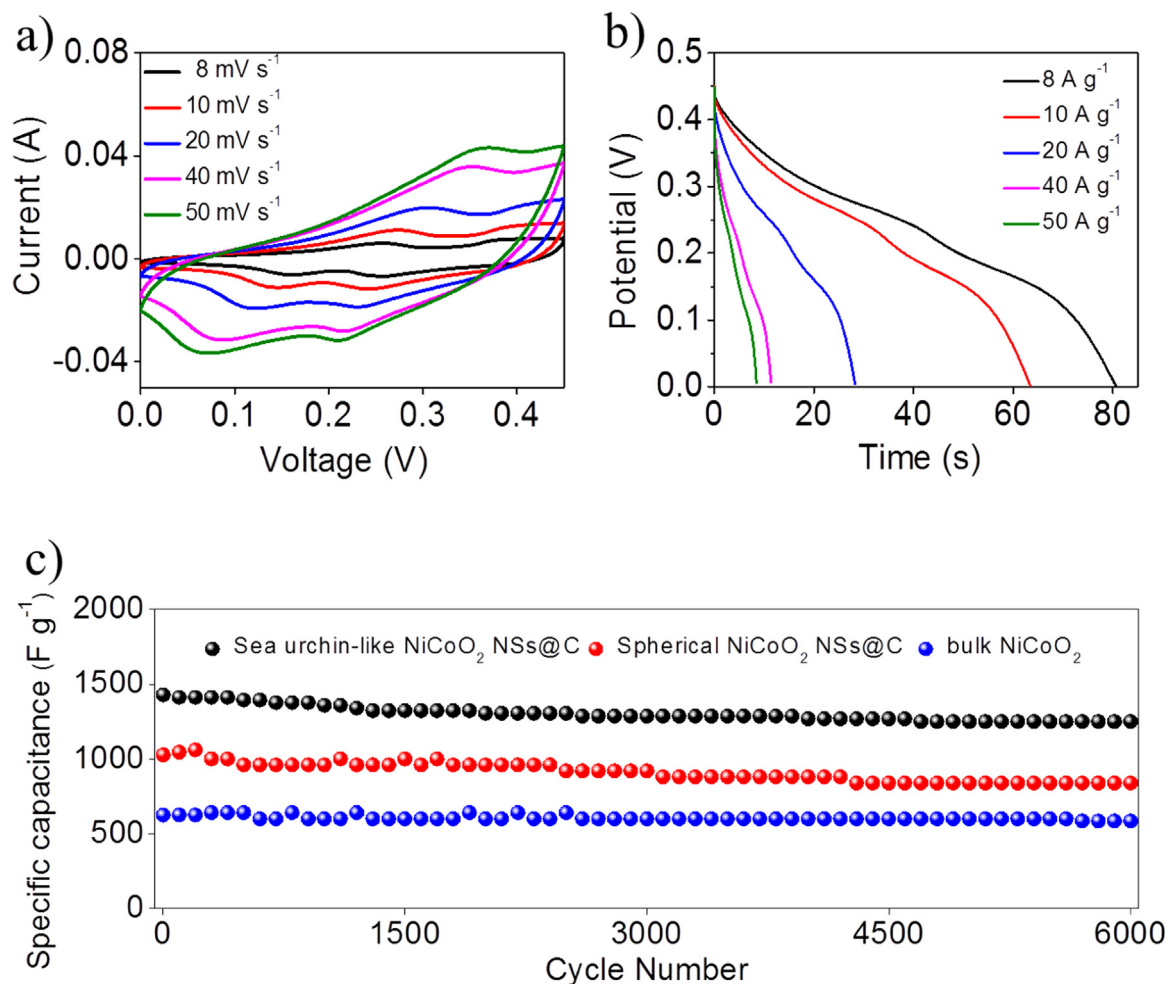


Fig. 5. (a) Cyclic voltammograms of sea urchin-like NiCoO_2 NSs@C composites at 8, 10, 20, 40 and 50 mV s^{-1} ; (b) Galvanostatic charge-discharge voltage profiles of sea urchin-like NiCoO_2 NSs@C composites at 8, 10, 20, 40 and 50 A g^{-1} ; (c) Cycling performance of sea urchin-like NiCoO_2 NSs@C, spherical NiCoO_2 NSs@C composites and bulk NiCoO_2 .

properties of the sea urchin-like NiCoO₂ NSs@C electrode materials in 2 M KOH solution between 0 and 0.45 V (vs SCE) at various current densities ranging from 8 to 50 A g⁻¹. All the curves in Fig. 5b are nonlinear, which further suggests the pseudocapacitance behavior of the sea urchin-like NiCoO₂ NSs@C composites. The specific capacitance at different current densities are measured by galvanostatic charge–discharge voltage profiles in Fig. 5b. The C_{sp} is calculated by following equations:

$$C_{sp} = I \cdot \Delta t / m \cdot \Delta V \quad (11)$$

where I is the discharge current, Δt assigned the discharge time, m is the active material mass, and ΔV is the electrochemical window (0.45 V).

As shown in Fig. S7, the special electrode delivers good pseudocapacitances of 1433, 1411, 1258, 1013 and 944 F g⁻¹ at 8, 10, 20, 40 and 50 A g⁻¹, respectively. It is worth noting that about 66% of the capacitance is retained after the charge–discharge current rate is raised from 8 to 50 A g⁻¹. The results confirm that this electrode can display high specific capacitance even at high current densities. In addition, the cycling performance of sea urchin-like NiCoO₂ NSs@C composites is examined as a significant parameter for the practical application. Fig. 5c illustrates the cycling life of sea urchin-like NiCoO₂ NSs@C composites, spherical NiCoO₂ NSs@C particles and block NiCoO₂ at a current density of 10 A g⁻¹. As expected, the capacity of block NiCoO₂ is unfavorable, while the other two electrodes seem to have shown relatively positive results. Interestingly, the initial specific capacitance is about 1429 and 1027.5 F g⁻¹ of sea urchin-like NiCoO₂ NSs@C composites, spherical NiCoO₂ NSs@C particles, respectively. After 6000 cycles, the corresponding specific capacitance decreases to 1250 and 840 F g⁻¹ with 87.5% and 81.8% retention. The hollow structure shows better results than a solid structure as reported in previous literature [52,53]. These results convincingly demonstrate that the electrochemical properties of sea urchin-like NiCoO₂ NSs@C composites are superior than hollow spherical NiCoO₂ NSs@C particles. Until now, such remarkable electrochemical performance has never been reported in batteries or supercapacitors based on Ni–Co materials [54–56].

The following reasons are advanced in the understanding of our results. 1) the homogeneous combination of ultrathin NiCoO₂ nanosheets with a hollow carbon substrate can effectively alleviate the physical strain, resulting in less break-up and pulverization of the active materials during the charge–discharge processes. 2) the ultrathin NiCoO₂ nanosheets with appropriate pore volume can offer convenient paths for charge-carrier transport between the electrolyte and active materials. The material synthesis allows facile penetration of the electrolyte, which can help promote the surface and near surface redox reaction during cycling [10]. Moreover, they can provide rich accessible electro-active sites, thus can facilitate the participation of the active material in redox for efficient energy storage, especially at relevant high rates [6,57]. 3) The highly-specific morphology and structure of the electrode architecture not only possesses the advantages from using nanosheet and hollow structures, but also by being more efficiently packed (Fig. S8) with improved interconnection between the particles, all combined together for offering remarkable enhancement in the electrochemical performance. Such a design strategy for electrode materials can be easily generalized to other nanoporous metal architectures, such as ZnO NSs@C (Fig. S9), Co₃O₄ NSs@C (Fig. S10) and CoFe₂O₄@C nanoparticles (Fig. S11).

3. Conclusion

We have designed a new hollow sea urchin-like structure combining the high conductivity of nanosheets with a mesoporous

concave carbon disk. As an electrode for Li-ion batteries, the composite material exhibits a reversible capacity of around 1210 mA h g⁻¹ at a current density of 0.4 A g⁻¹, retaining 913 mA h g⁻¹ after 200 cycles. In addition, a high specific capacitance of 944 F g⁻¹ at 50 A g⁻¹ with remarkable cycling stability (12.5% specific capacitance decay after 6000 cycles at 10 A g⁻¹) was achieved as an electrochemical supercapacitor electrode. The good electrochemical performance was considered to be attributed to the desirable composition and unique structure. It is possible that such synthetic strategies could be adopted to fabricate other binary or ternary metal oxide-based nanostructures. We also anticipate these electrode materials can be applied in many energy storage devices.

4. Experimental section

4.1. Synthesis of hollow concave sulfonated polystyrene (SPS) templates

All the chemicals were directly used after purchase without further purification. The hollow concave polystyrene (PS) particles were obtained according to a reported method [7]. 35 mL of concentrated sulfuric acid and 2 g of PS were mixed for 30 min at 40 °C. After that, the precipitate was collected by centrifugation and washed with ice water and ethanol. As a result, primrose yellow hollow concave SPS templates were obtained.

4.2. Synthesis of sea urchin-like NiCoO₂ NSs@C hybrid structure

For the typical synthesis of the NiCoO₂ NSs@C hybrid structure, 50 mg of the hollow concave SPS powder was first mixed with 40 mL of deionized water dissolved with 0.25 mM of nickel nitrate hexahydrate (Ni(NO₃)₂·6H₂O), 0.5 mM of cobalt nitrate hexahydrate (Co(NO₃)₂·6H₂O), 0.25 mM of hexamethylenetetramine (C₆H₁₂N₄) and 0.025 mM of trisodium citrate. In order to achieve a homogeneous dispersion, the upper solution was sonicated for 15 min. Then, the solution was heated up to 90 °C in an oil bath with stirring. After reaction for 9 h, the Ni–Co precursor@SPS hybrid was collected by centrifugation. Then, the samples were washed by deionized water and ethanol several times after the solution was cooled to room temperature (25 °C) naturally. After annealing the Ni–Co precursor@SPS at 450 °C for 3 h in nitrogen at a heating rate of 1 °C min⁻¹, the sea urchin-like NiCoO₂ NSs@C hybrid structure was formed. Significantly, it is also a general principle to control the size and thickness of the nanosheets by regulating the concentration of HMT and SCT, displayed in Fig. S12.

4.3. Synthesis of spherical hollow NiCoO₂ NSs@C sphere

Spherical hollow NiCoO₂ NSs@C spheres were prepared by a similar procedure using hollow PS spheres without any treatment of the template so that the two morphologies can be compared.

4.4. Synthesis of bulk NiCoO₂ flake

Bulk NiCoO₂ flakes were prepared by a similar procedure with 0.25 mmol of cobalt nitrate hexahydrate (Co(NO₃)₂·6H₂O) and without using any template.

4.5. Materials characterization

The composition and crystal structure were characterized by X-ray diffraction (XRD; SHIMADZU, Lab X XRD-6000). Thermogravimetric analysis (PerkinElmer TGA 7) was carried out under air with a temperature ramp of 10 °C min⁻¹ from room temperature

to 600 °C. The Raman spectra was measured on a Raman spectrometer under a backscattering geometry ($k=633$ nm; HORIBA JOBIN YVON, HR 800). And the specific surface area and pore size distribution data of samples were performed by a BET analyzer (Autosorb-iQ, Quantachrome Instruments U.S.) at 77 K. Field-emission scanning electron microscopy (FESEM) images were gained by a HITACHI SU-8010 microscope. Transmission electron microscopy (TEM) and selected area electron diffraction (SAED) images were obtained on a JEOL JEM-2100F microscope.

4.6. Electrochemical measurements

Lithium-ion battery performance test The electrochemical behavior of the sea urchin-like NiCoO₂ NSs@C hybrid composite was performed using CR2025 coin-type cells assembled in an glove box (Dellix, [O₂] < 1 ppm, [H₂O] < 1 ppm) in argon with lithium serving as the anode. The working electrode was prepared by compressing a mixture of active materials, conductive material (carbon black, C-ENERGYTM Super C65), and binder (poly-vinylidene fluoride, PVDF) in a weight ratio of 70:20:10 and pasted on Cu foil ($D=12.6$ mm) current collector, drying at 80 °C for 24 h and then dried at 120 °C overnight under vacuum. The loading mass of active materials is about 0.8 mg cm⁻². The relative digital photo and SEM images are shown in Fig. S13. The electrolyte used was a mixture of ethylene carbonate and dimethyl carbonate (EC/DMC) (1:1 in volume) containing 1 M LiPF₆. Microporous membrane (PP/PE/PP) from Celgard was used as the separator. Cyclic voltammetry was performed using an electrochemical workstation (CHI 660D). Galvanostatic discharge/charge cycles were tested on a NEWARE battery tester over a voltage range of 3.0–0.01 V at room temperature (25 °C).

Supercapacitor property test The prepared slurry was pressed onto nickel foam (1*1 cm²) with loading mass of 1.2 mg cm⁻². The capacitive performance was tested on a CHI 660D electrochemical workstation with cyclic voltammetry and chronopotentiometry functions using a three-electrode cell where Pt foil serves as the counter electrode and a standard calomel electrode (SCE) as the reference electrode. The distance between the working electrode and the counter electrode is about 0.5 cm.

Acknowledgements

This work was supported by the National Natural Science Foundation of China (No. 51273158 and 21303131), Natural Science Basis Research Plan in Shaanxi Province of China (No. 2012JQ6003), and Program for New Century Excellent Talents in University (NCET-13-0449). This work was also supported by the U.S. Department of Energy under Contract DE-AC0206CH11357 with the support provided by the Vehicle Technologies Office, Department of Energy (DOE) Office of Energy Efficiency and Renewable Energy (EERE).

Appendix A. Supplementary material

Supplementary data associated with this article can be found in the online version at <http://dx.doi.org/10.1016/j.nanoen.2016.06.032>.

References

- [1] L. Schlapbach, A. Züttel, *Nature* 414 (2001) 353–358.
- [2] S.M. Hasnain, *Energy Convers. Manag.* 39 (1998) 1127–1138.
- [3] P. Simon, Y. Gogotsi, *Nat. Mater.* 7 (2008) 845.
- [4] X. Li, X. Meng, J. Liu, D. Geng, Y. Zhang, M.N. Banis, Y. Li, J. Yang, R. Li, X. Sun, *Adv. Funct. Mater.* 22 (2012) 1647–1654.
- [5] H. Fu, Z.-j. Du, W. Zou, H.-q. Li, C. Zhang, *Carbon* 65 (2013) 112–123.
- [6] J. Liang, Z. Fan, S. Chen, S. Ding, G. Yang, *Chem. Mater.* 26 (2014) 4354–4360.
- [7] J. Liang, X.-Y. Yu, H. Zhou, H.B. Wu, S. Ding, X.W. Lou, *Angew. Chem. Int. Ed.* 53 (2014) 12803–12807.
- [8] P.L. Taberna, S. Mitra, P. Poizot, P. Simon, J.M. Tarascon, *Nat. Mater.* 5 (2006) 567–573.
- [9] G. Tan, F. Wu, Y. Yuan, R. Chen, T. Zhao, Y. Yao, J. Qian, J. Liu, Y. Ye, R. Shahbazian-Yassar, J. Lu, K. Amine, *Nat. Commun.* 7 (2016) 11774.
- [10] H.B. Wu, H. Pang, X.W. Lou, *Energy Environ. Sci.* 6 (2013) 3619–3626.
- [11] C. Yuan, H.B. Wu, Y. Xie, X.W. Lou, *Angew. Chem. Int. Ed.* 53 (2014) 1488–1504.
- [12] G.Q. Zhang, H.B. Wu, H.E. Hoster, M.B. Chan-Park, X.W. Lou, *Energy Environ. Sci.* 5 (2012) 9453–9456.
- [13] G. Zhang, B.Y. Xia, X. Wang, X.W. Lou, *Adv. Mater.* 26 (2014) 2408–2412.
- [14] L. Shen, L. Yu, X.-Y. Yu, X. Zhang, X.W. Lou, *Angew. Chem. Int. Ed.* 54 (2015) 1868–1872.
- [15] D.P. Dubal, P. Gomez-Romero, B.R. Sankapal, R. Holze, *Nano Energy* 11 (2015) 377–399.
- [16] H. Guo, T. Li, W. Chen, L. Liu, X. Yang, Y. Wang, Y. Guo, *Nanoscale* 6 (2014) 15168–15174.
- [17] R. Ding, L. Qi, H. Wang, *J. Solid State Electrochem.* 16 (2012) 3621–3633.
- [18] C. Yuan, J. Li, L. Hou, X. Zhang, L. Shen, X.W.D. Lou, *Adv. Funct. Mater.* 22 (2012) 4592–4597.
- [19] B. Cui, H. Lin, J.B. Li, X. Li, J. Yang, J. Tao, *Adv. Funct. Mater.* 18 (2008) 1440–1447.
- [20] L. Huang, D. Chen, Y. Ding, S. Feng, Z.L. Wang, M. Liu, *Nano Lett.* 13 (2013) 3135–3139.
- [21] X. Liu, S. Shi, Q. Xiong, L. Li, Y. Zhang, H. Tang, C. Gu, X. Wang, J. Tu, *ACS Appl. Mater. Inter.* 5 (2013) 8790–8795.
- [22] Y. Idota, T. Kubota, A. Matsufuji, Y. Maekawa, T. Miyasaka, *Science* 276 (1997) 1395–1397.
- [23] S.H. Ng, J. Wang, D. Wexler, K. Konstantinov, Z.P. Guo, H.K. Liu, *Angew. Chem. Int. Ed.* 45 (2006) 6896–6899.
- [24] R. Ryoo, S.H. Joo, M. Kruk, M. Jaroniec, *Adv. Mater.* 13 (2001) 677–681.
- [25] B. Dong, X. Zhang, X. Xu, G. Gao, S. Ding, J. Li, B. Li, *Carbon* 80 (2014) 222–228.
- [26] R.H. Baughman, A.A. Zakhidov, W.A. de Heer, *Science* 297 (2002) 787–792.
- [27] J. Song, G. Li, K. Xi, B. Lei, X. Gao, R.V. Kumar, *J. Mater. Chem. A* 2 (2014) 10041–10047.
- [28] X. Xu, H. Tan, K. Xi, S. Ding, D. Yu, S. Cheng, G. Yang, X. Peng, A. Fakeeh, R. V. Kumar, *Carbon* 84 (2015) 491–499.
- [29] K. Xi, B. Chen, H. Li, R. Xie, C. Gao, C. Zhang, R.V. Kumar, J. Robertson, *Nano Energy* 12 (2015) 538–546.
- [30] G.-C. Cho, J. Dodds, J.C. Santamarina, *J. Geotech. Geoenviron.* 132 (2006) 591–602.
- [31] K. Saravanan, K. Ananthanarayanan, P. Balaya, *Energy Environ. Sci.* 3 (2010) 939–948.
- [32] J. Liang, H. Hu, H. Park, C. Xiao, S. Ding, U. Paik, D.X.-W. Lou, *Energy Environ. Sci.* 8 (2015) 1707–1711.
- [33] C.W. Lee, S.-D. Seo, D.W. Kim, S. Park, K. Jin, D.-W. Kim, K.S. Hong, *Nano Res* 6 (2013) 348–355.
- [34] K. Chang, D. Geng, X. Li, J. Yang, Y. Tang, M. Cai, R. Li, X. Sun, *Adv. Energy Mater.* 3 (2013) 839–844.
- [35] C. Wang, W. Wan, Y. Huang, J. Chen, H.H. Zhou, X.X. Zhang, *Nanoscale* 6 (2014) 5351–5358.
- [36] C. Yuan, J. Li, L. Hou, X. Zhang, L. Shen, X.W. Lou, *Adv. Funct. Mater.* 22 (2012) 4592–4597.
- [37] X. Xu, H. Zhou, S. Ding, J. Li, B. Li, D. Yu, *J. Power Sources* 267 (2014) 641–647.
- [38] J.S. Chen, X.W. Lou, *Small* 9 (2013) 1877–1893.
- [39] H.J. Peng, J.Q. Huang, M.Q. Zhao, Q. Zhang, X.B. Cheng, X.Y. Liu, W.Z. Qian, F. Wei, *Adv. Funct. Mater.* 24 (2014) 2772–2781.
- [40] F. Zhang, D. Zhu, Q. Chen, *ACS Appl. Mater. Inter.* 6 (2014) 9256–9264.
- [41] G. Tan, F. Wu, J. Lu, R. Chen, L. Li, K. Amine, *Nanoscale* 6 (2014) 10611–10622.
- [42] H.S. Jadhav, R.S. Kalubarme, C.-N. Park, J. Kim, C.-J. Park, *Nanoscale* 6 (2014) 10071–10076.
- [43] X. Xu, B. Dong, S. Ding, C. Xiao, D. Yu, *J. Mater. Chem. A* 2 (2014) 13069–13074.
- [44] P. Lian, X. Zhu, H. Xiang, Z. Li, W. Yang, H. Wang, *Electrochim. Acta* 56 (2010) 834–840.
- [45] J. Li, S. Xiong, Y. Liu, Z. Ju, Y. Qian, *ACS Appl. Mater. Interfaces* 5 (2013) 981–988.
- [46] Z.-S. Wu, W. Ren, L. Wen, L. Gao, J. Zhao, Z. Chen, G. Zhou, F. Li, H.-M. Cheng, *ACS Nano* 4 (2010) 3187–3194.
- [47] Y. He, X. Yu, Y. Wang, H. Li, X. Huang, *Adv. Mater.* 23 (2011) 4938–4941.
- [48] Y.S. Jung, A.S. Cavanagh, L.A. Riley, S. Kang, A.C. Dillon, M.D. Groner, S. M. George, S.H. Lee, *Adv. Mater.* 22 (2010) 2172–2176.
- [49] K. Chang, W. Chen, *ACS Nano* 5 (2011) 4720–4728.
- [50] X. Zhang, S. Yu, W. He, H. Uyama, Q. Xie, L. Zhang, F. Yang, *Biosens. Bioelectron.* 55 (2014) 446–451.

- [51] X. Wang, C. Yan, A. Sumboja, P.S. Lee, J. Nanosci. Nanotechnol. 14 (2014) 7104–7110.
- [52] G. Zhou, J. Zhu, Y. Chen, L. Mei, X. Duan, G. Zhang, L. Chen, T. Wang, B. Lu, Electrochim. Acta 123 (2014) 450–455.
- [53] L. David, R. Bhandavat, G. Singh, ACS Nano 8 (2014) 1759–1770.
- [54] Y. Luo, H. Zhang, D. Guo, J. Ma, Q. Li, L. Chen, T. Wang, Electrochim. Acta 132 (2014) 332–337.
- [55] I. Shakir, Electrochim. Acta 132 (2014) 490–495.
- [56] J. Xiao, S. Yang, J. Mater. Chem. 22 (2012) 12253–12262.
- [57] J. Liang, B. Dong, S. Ding, C. Li, B.Q. Li, J. Li, G. Yang, J. Mater. Chem. A 2 (2014) 11299–11304.